Journal of Materials Chemistry C

ROYAL SOCIETY OF CHEMISTRY

COMMUNICATION

View Article Online
View Journal

Cite this: DOI: 10.1039/d5tc02239h

Received 10th June 2025,
Accepted 17th July 2025

DOI: 10.1039/d5tc02239h

rsc.li/materials-c

Switching of light responsive metal–organic gels from insulator to semiconductor: flexible smart semiconducting membranes for optoelectronic device fabrication†

Mouli Das Dawn,[a] Someprosad Patra,[b] Debamalya Banerjee[b] and Kumar Biradha *[a]

In the era of artificial intelligence and machine learning, semiconductor materials are the foundation of contemporary electronics and are essential for advancing technological innovation in widespread fields. Herein, we report a Ni-MOG (1) that undergoes gel-to-gel transformation, upon photochemical stimuli, *via* [2+2] reaction. It associates with the most spectacular change of green to yellow MOG (1′). Both the MOGs have shown an excellent ability to absorb nitrate salts of metals (M = Li, Mg) and transform to even stronger gels (1@M, 1′@M). The 1′@Li-MOG was found to be the strongest as the rigidity increased 51-fold. Our studies on their conductivity indicate that incorporation of metal-salts into MOGs significantly enhances the conductivity, and they are otherwise insulators. Furthermore, MOG 1′@Li was found to exhibit the highest conductivity compared to 1@Mg, 1@Li, and 1′@Mg, in any of the three forms of measurement: pelleted, thin-film, and integration with mixed-matrix-membrane (MMM). The integration of Li-doped irradiated MOG with MMM exhibited the highest lithium-ion conductivity of 6.11 × 10^{-2} S cm^{-1} among all MOF/MOG-based materials. The ability of these materials to power LEDs highlights their potential for optoelectronic applications. We note here that these are the first reports of MOGs that transitioned from insulators to semiconductors upon undergoing [2+2] reaction and subsequent Li-doping.

1. Introduction

Semiconducting materials form the backbone of modern electronics in the age of artificial intelligence and machine learning, and play a crucial role in driving progress and innovation across various technological applications.[1,2] The advent of modern technology has significantly transformed the way we communicate, calculate, and traverse our daily lives through the discovery and manipulation of semiconductors.[3] Semiconductors, usually crystalline solids with a small band gap, are distinguished by their ability to conduct electricity under certain conditions, making them ideal for use in electronic devices like light-emitting diodes (LED).[4] Consequently, modern scientific research has concentrated on developing semiconducting materials that fulfill the demands of current technology while remaining cost-effective and easy to produce. Several potential materials such as graphene,[5] metals,[6] organic polymers,[7] carbon nanotubes,[8] metal oxides,[9] and metallic alloys,[10] are being actively investigated for their potential applications as semiconducting materials. We previously reported a photoswitchable and photoluminescent organic semiconductor based on cation–π and carboxylate–pyridinium interactions.[11] In this context, metal–organic gels (MOGs) are a class of semi-solid, viscoelastic supramolecular coordination polymers that have emerged over the past two decades. These materials offer unique advantages, such as stability, self-sustainability, and porosity.[12–15]

MOGs are typically created through the judicious choice of metal salts, organic ligands, solvents and subtle tuning of the reaction conditions for their self-assembly process.[16–18] Most synthetic gels exist in a "kinetically trapped state" and lack autonomous behavior unless externally disrupted.[19–23] Under specific conditions, certain supramolecular gels can adapt and reconfigure their material properties in response to remote, non-invasive external stimuli.[24–28] Gelator molecules can transition into different assemblies, such as another gel,[29,30] a crystal,[31,32] or a micellar non-gel phase,[33] in response to external stimuli. These transitions are often accompanied by changes in the material's rigidity, color, viscosity, morphological structure, and photophysical properties.[34–39]

The exploration of gels to facilitate organic topochemical reactions and catalysis is gaining popularity among chemists. To date, only a limited number of self-assembled gelators have been reported to undergo topochemical reactions such as [2+2], [4+4], [4+2], and [1,4]-addition reactions in the gel state.[40–51]

[a] Department of Chemistry, Indian Institute of Technology Kharagpur, Kharagpur 721302, India. E-mail: kbiradha@chem.iitkgp.ac.in
[b] Department of Physics, Indian Institute of Technology Kharagpur, Kharagpur 721302, India

† Electronic supplementary information (ESI) available. See DOI: https://doi.org/10.1039/d5tc02239h

Recently, we demonstrated the first example of a gel-to-gel transformation *via* [2+2] photopolymerization in MOGs composed of metal halides and rigid dienes.[52] MOGs are highly significant owing to their various applications in catalysis, sensing, gas storage, and optics.[53–55] Despite their potential, only a limited number of studies have explored tuning metallogel properties through the incorporation of alkali and alkaline earth metal ions into the gel matrix. Recently, alkali and alkaline earth metal cation-assisted self-assembly has garnered attention for fabricating metal–organic assembly-based smart materials with various applications.[56]

The ability to incorporate large amounts of dopants and achieve high electrical conductivity has gained interest for thermoelectric applications.[57,58] Doping modifies a semiconductor's electrical properties, as seen in MOGs like $[M(DTA)]_n$ (M: Ni, Cu, Pd), where exposure to I_2 vapor enhanced conductivity to 10^{-5} S cm^{-1}.[59] However, alkali/alkaline earth metal doping in photoreactive MOGs remains underexplored. Coordination networks with functional organic ligands form porous architectures in MOGs similar to metal–organic frameworks (MOFs).[60–63] Studies on Li^+, Na^+, and Mg^{2+} ion-conducting MOFs *via* post-synthetic modification show promising results. Long *et al.* (2011) reported the first MOF-based solid electrolyte with 3.1×10^{-4} S cm^{-1} conductivity at 300 K.[64] Park *et al.* demonstrated that Li^+ doping in the Cu–azolate MOF improved the conductivity from 10^{-14} to 10^{-4} S cm^{-1}.[65] Similarly, our work on Li–AOIA–MOF demonstrated that Li^+ doping results in a 183-fold increase, reaching 1.09×10^{-5} S cm^{-1}.[66] ZIF-67@ZIF-8, which can store more lithium ions and transmit them by the wall of the cavity, exhibited significant ionic conductivity (1.35×10^{-3} S cm^{-1} at 25 °C).[67] Additionally, MIL-Al@$LiClO_4$ represents a new class of pseudo-solid-state lithium-ion conducting electrolytes, exhibiting a conductivity of 1.22×10^{-3} S cm^{-1}.[68]

The conductivity of many of the Li^+-doped MOFs is typically measured in pellet form, limiting their practical applications due to fragility and grain boundary issues that hinder conductivity. Two strategies are in use to address these challenges: (a) device fabrication on ITO glass (thin-film) and (b) mixed-matrix membranes (MMMs). Thin films are widely used in semiconductors, solar panels, and optical devices, providing enhanced conductivity.[69] MMMs have the potential to synergistically combine the organic and inorganic materials, enabling continuous charge transfer pathways for semiconductive membranes. Given the lack of research on alkali/alkaline earth metal-based dopants in photoreactive MOGs and their scalable synthesis, we focused on developing thin-film and MMM-based semiconducting gels for practical applications.

We report the first-ever transparent thixotropic photoreactive Ni-MOG undergoing gel-to-gel transformation *via* [2+2] reaction, with the most striking color change from green to yellow. Conductivity measurements before and after irradiation show values around 10^{-10} S cm^{-1}, placing it among the least conductive materials, near the insulator range. To achieve the highest possible conductivity, we adopted a doping strategy using $LiNO_3$ and $Mg(NO_3)_2$ salts. Most notably, lithium salt uptake led to an unprecedented 51-fold increase in gel rigidity. The conductivities of the doped materials were analyzed in three ways: (a) pelletized form, (b) device fabrication on ITO glass, and (c) mixed matrix membrane fabrication. Our studies suggest that the thin films and mixed matrix membranes exhibit the most significant conductivity improvement compared to that of the pelleted form. The MMM containing Li-doped irradiated MOG was found to display the highest lithium-ion conductivity of 6.11×10^{-2} S cm^{-1} compared with all reported Li-doped MOF/MOG-based materials. These are the first reports of MOG materials that converted from an insulator to a semiconductor upon undergoing photochemical reaction and subsequent Li doping. The fabricated device demonstrates the greatest potential for commercial applications by successfully lighting LEDs.

2. Results and discussion

The pyridine and imidazo-pyridine substituted olefin, **L**, was synthesized by the condensation reaction of 4-pyridylacrylic acid with 3,4-diaminopyridine in the presence of polyphosphoric acid.[32] The aqueous solution of $Ni(CH_3COO)_2$, when mixed with the methanol solution of **L** at room temperature, formed a transparent green gel, Ni-MOG (**1**), within three hours. The formation of a rigid gel was confirmed using the inverted vial method (Scheme S1, ESI†). This gel can be synthesized on a larger scale (100 g) and remains stable under ambient conditions for over eight months (Fig. S1, ESI†). It exhibits thixotropic behavior, transitioning between gel and sol with mechanical agitation and rest. It is also thermo-reversible, liquefying when heated and solidifying upon cooling (Fig. S2, ESI†). Chemical stimuli such as HCl, NH_3, or EDTA also triggered gel-to-sol transitions (Fig. S3, ESI†). The mechanical strength of Ni-MOG was assessed through rheological experiments under ambient conditions, which showed that the storage modulus (G') remained consistently higher than the loss modulus (G'') across all measured points, confirming its robust gel-like nature (Fig. 1a and b). The gel exhibited a yield stress (σ_y) of 17 Pa and a G'–G'' value of 5885 Pa. A time-dependent step-strain hysteresis loop test over five cycles at 10 rad s^{-1} confirmed its thixotropic behavior (Fig. S4, ESI†). Gelation capability was tested in various solvents, including ethanol, *n*-propanol, and longer-chain alcohols. However, the gel formation of **L** with $Ni(CH_3COO)_2$ was found to occur only up to *n*-propanol (Fig. S5, ESI†). Rheological studies showed that gel strength decreased with increasing alcohol chain length (Table S1, ESI†). Acetate ions were also found to play a crucial role in gelation, as the reactions with $Ni(NO_3)_2$, $Ni(ClO_4)_2$, and $NiCl_2$ produced clear solutions, and $NiSO_4$ formed a precipitate (Fig. S6, ESI†). The xerogel (1-XG) was obtained by freeze-drying the gelatinous material.

The composition and morphology of **1** were analyzed using FESEM, TEM, EDAX, elemental mapping, IR spectroscopy, Raman spectroscopy, PXRD, XPS, and solid-state UV-vis spectroscopy. FESEM and TEM images revealed a typical cross-linked fibrous network (Fig. 1c and d), while elemental

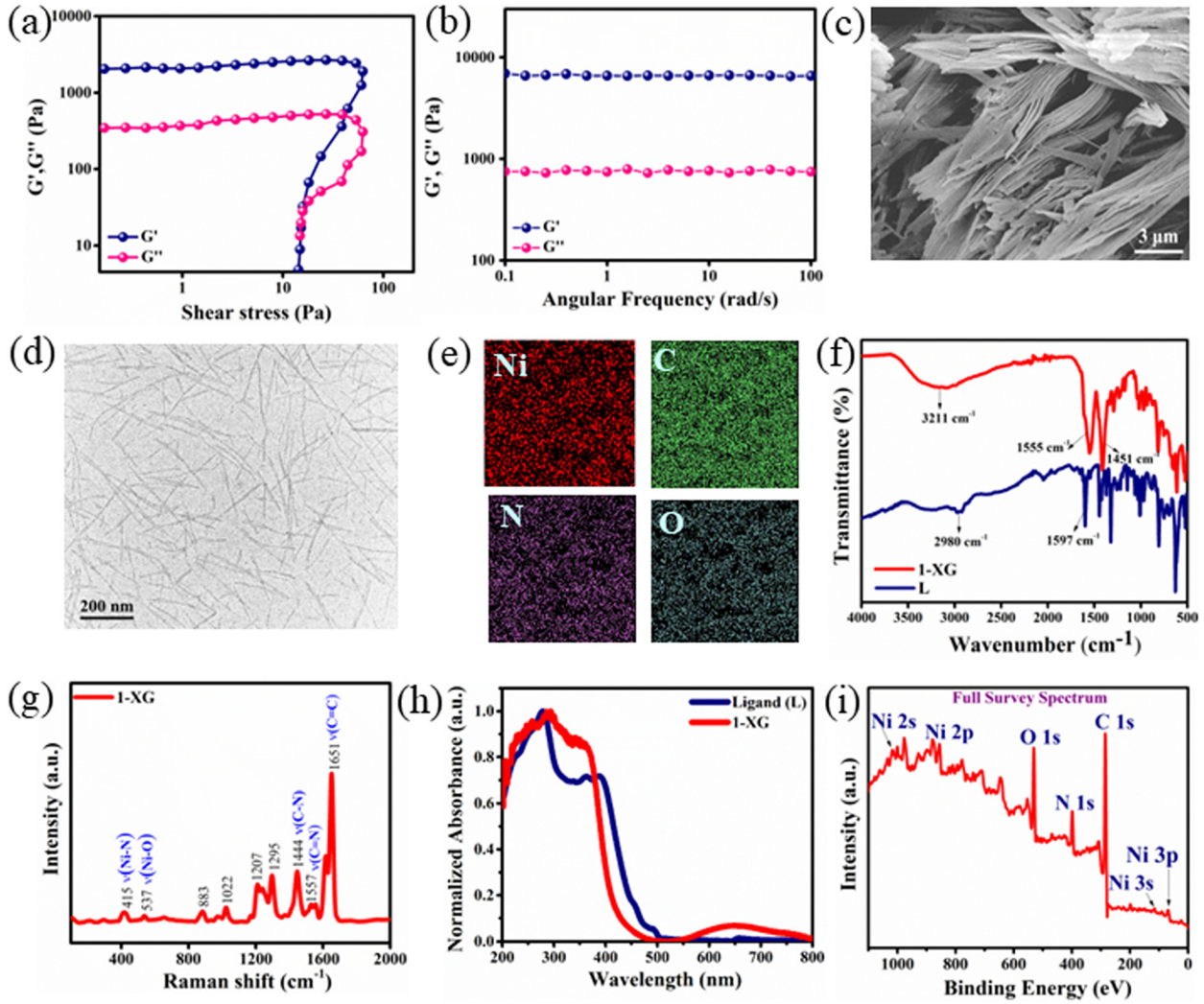

Fig. 1 Variation of storage modulus (G') and loss modulus (G'') of **1** with (a) shear stress and (b) frequency; (c) FESEM image; (d) TEM image; (e) elemental mapping; (f) FTIR spectra (g) Raman spectra; (h) solid-state UV-vis spectroscopy; (i) full survey spectrum of XPS analysis of **1**.

mapping and EDAX analysis showed a homogeneous metal ion distribution (Fig. 1e and Fig. S7, ESI†). The PXRD pattern lacked prominent peaks, confirming the amorphous nature of **1**-XG (Fig. S8, ESI†). The solid-state UV-vis spectrum displayed an absorption peak at 650 nm, attributed to charge transfer between the ligand and Ni^{2+}, indicating a hexacoordinated high-spin Ni^{2+} in a distorted octahedral geometry (Fig. 1h). IR spectral analysis provided insights into coordination and hydrogen bonding (Fig. 1f). The free ligand exhibited an imidazole –NH peak at 2980 cm^{-1}, which disappeared in **1**-XG, replaced by a broad peak (3057–3541 cm^{-1}), confirming hydrogen bonding with solvent molecules. The C═N stretching of pyridyl moieties shifted from 1597 cm^{-1} (**L**) to 1555 cm^{-1} (**1**-XG), consistent with metal coordination.[70] In addition, **1**-XG also displayed a peak at 1451 cm^{-1}, corresponding to the methyl CH bending of acetate in the MOG. Raman spectra revealed characteristic ligand vibrations (~1444 cm^{-1}, ~1557 cm^{-1}, ~1651 cm^{-1}) and Ni–N symmetric stretching at 415 cm^{-1} (Fig. 1g). XPS analysis confirmed the presence of C, N, O, and Ni, with Ni $2p_{3/2}$ and Ni $2p_{1/2}$ peaks at 855.4 eV and 873.12 eV, plus satellite peaks at 864.65 eV and 883.50 eV, indicating Ni(II) ions (Fig. 1i and Fig. S9, ESI†). Deconvolution identified Ni–N and Ni–O bonds, with N 1s peaks at 399.3 eV and 400.9 eV corresponding to Ni–N and C═N bonding. O 1s and C 1s spectra confirmed Ni–O, C═O, and water coordination, with H-bonding among **L**, Ni(II), acetate ions, and water driving gel formation.

To investigate the photochemical [2+2] reactivity, freshly prepared gel material was placed in a 15 mL vial and irradiated under UV-A light (315–400 nm). The reaction was monitored at various time intervals by recording ^{1}H NMR in DMSO-d_6 (Fig. S10, ESI†). Since the irradiated material was insoluble in DMSO, it was treated with ~25% aqueous ammonia overnight to remove metal ions. The ^{1}H NMR spectra of the irradiated MOG (**1′**) showed new peaks at 4.90–5.06 ppm (Fig. 2c), confirming cyclobutene proton formation. The monomer peak at 13.21 ppm disappeared after five days, indicating 100% conversion. The imidazole protons in **1′** shifted to 12.61 ppm, confirming intact imidazole functionality. Remarkably, **1**

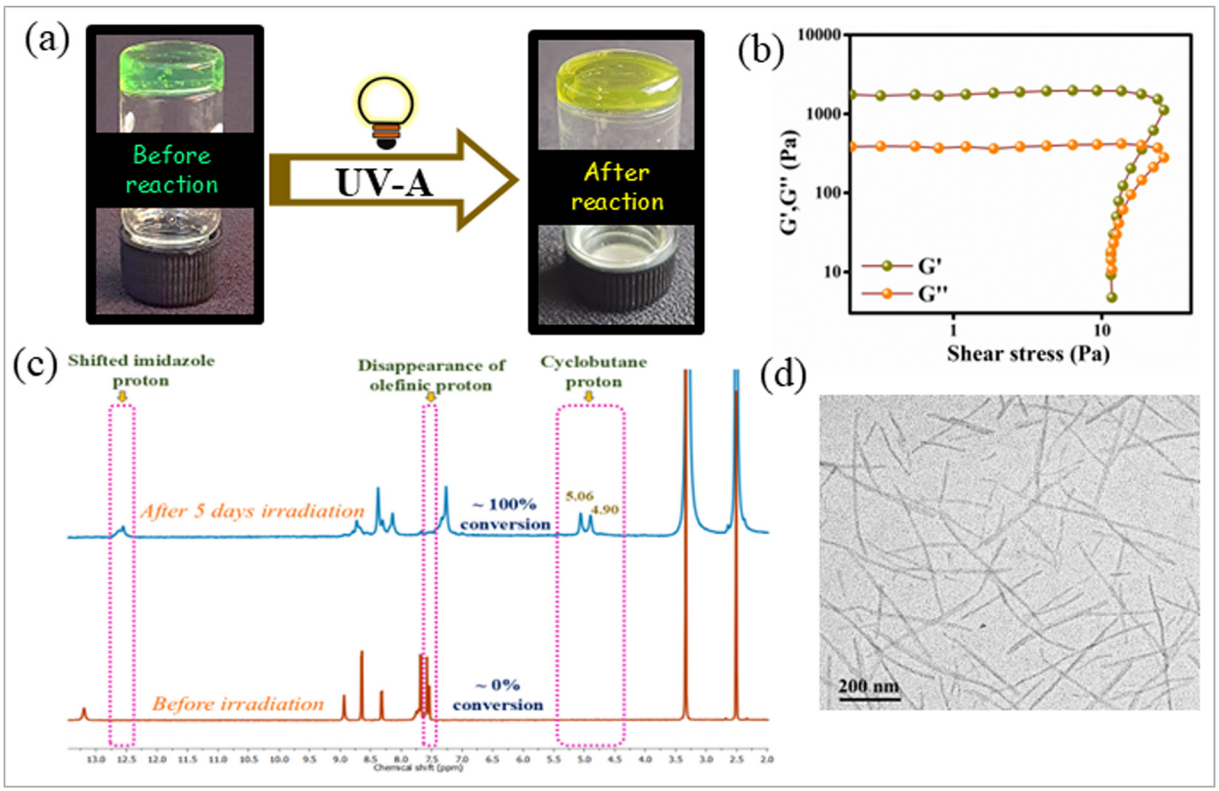

Fig. 2 Illustrations of gel-to-gel transformations *via* [2+2] photoreaction of **1**: (a) inverted vial test before and after [2+2] reaction; (b) dependence of storage modulus (G') and loss modulus (G'') on shear stress of **1′**; (c) ^{1}H NMR spectra of **1** and **1′** in DMSO-d_6; (d) TEM image of **1′**.

retained its gelatinous nature throughout the complete conversion of **L** to its corresponding dimer. The rigid gelatinous nature of **1′** was supported by the inversion vial test. Furthermore, the photoreactivity was evident through a significant color change of green to yellow (Fig. 2a). Rheological studies revealed altered mechanical properties post-photoreaction, with yield stress (σ_y) decreasing to 11.75 Pa and firmness (G'–G'') measured at 523 Pa (Fig. 2b and Fig. S11a and b, ESI†). FESEM and TEM images further confirmed that **1′** maintained its fibrous morphology (Fig. S11c (ESI†) and Fig. 2d), reinforcing the structural stability of the photoreacted gel.

The gels exhibited a remarkable ability to gradually absorb metal ions from methanolic solutions. To evaluate this, gels **1** and **1′** were immersed in nitrate salt solutions of Li, Mg, and Al to obtain **1**@Li & **1′**@Li, **1**@Mg & **1′**@Mg, and **1**@Al & **1′**@Al. Exposure to aluminium nitrate caused both gels (**1** and **1′**) to break down immediately, forming a precipitate, likely due to the corrosive nature of Al^{3+}.[71] However, when treated with lithium and magnesium nitrate, the gels were found to maintain their gelatinous nature with no sol formation (Fig. S12, ESI†). The effect of the absorption of various metal cations on gelation behavior has been reported for several protein gels, including Inca peanut albumin, soybean protein gels, and potato protein gels.[71–73] Such gel-to-gel transformations by the uptake of alkali–alkaline earth metal ions are scarcely documented for photoreacted MOGs. The addition of lithium and magnesium salts significantly enhanced the gel strength of both **1** and **1′** (Fig. S13–S16, ESI†). Rheological studies demonstrated substantial increases in firmness and rigidity (G'–G''), with enhancements of approximately 2.14-, 1.29-, 51-, and 38.8-fold for **1**@Li, **1**@Mg, **1′**@Li, and **1′**@Mg, respectively, compared to their parent gels (Fig. 3a). The yield stress (σ_y), a key indicator of gel strength, increased to 238 Pa (14-fold), 172 Pa (10-fold), 259 Pa (22-fold), and 230 Pa (19.57-fold) for **1**@Li, **1**@Mg, **1′**@Li, and **1′**@Mg, respectively (Fig. S17, ESI†). The thixotropic behavior of metal ion-doped gels was assessed by applying alternating strain amplitudes at a constant oscillation frequency of 10 rad s^{-1}, revealing rapid transitions between solid-like and liquid-like states over five cycles (Fig. S13c, S14c, S15c and S16c, ESI†). Lithium salts exhibited a stronger reinforcing effect than magnesium, likely due to greater Li^+ uptake. ICP-MS analysis confirmed this, measuring Li content at 3.26 wt% for **1′**@Li and 2.59 wt% for **1**@Li, compared to Mg content at 1.93 wt% for **1′**@Mg and 1.09 wt% for **1**@Mg. FESEM imaging further verified that the fibrous network of the MOGs remained intact after metal salt doping (Fig. 3b, c and Fig. S18, ESI†). EDAX and elemental mapping also confirmed the uniform distribution of all elements (Fig. 3d and Fig. S19–S21, ESI†). Notably, this study represents the first reported instance of a photoreactive gel achieving a remarkable 51-fold increase in rigidity upon lithium doping.

The optical properties of these materials were analyzed using UV-vis spectrophotometry (200–800 nm). The optical band gap energies, calculated using Tauc's equation, were

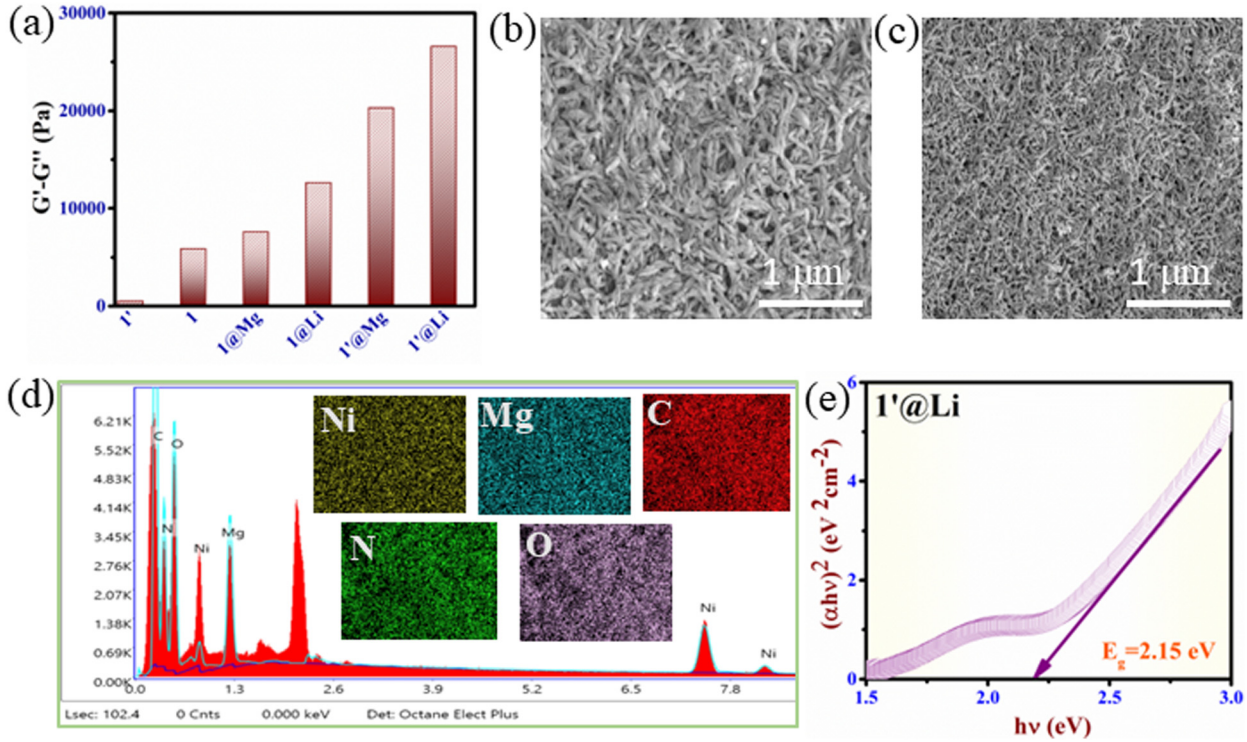

Fig. 3 (a) Comparison of gel rigidity before and after uptake of Li and Mg in **1** and **1**′; FESEM image of (b) **1**′@Li and (c) **1**′@Mg; (d) EDAX analysis and elemental mapping of **1**′@Mg; (e) Tauc's plot of **1**′@Li.

3.12 eV for **1**-XG and 3.03 eV for **1**′-XG. Doping with $LiNO_3$ and $Mg(NO_3)_2$ led to a reduction in band gap values, a change that was more pronounced with MOG **1**′. The lowest band gap, 2.15 eV, was observed for **1**′@Li (Fig. 3e). The band gap values followed the order of **1** > **1**′ > **1**@Mg > **1**@Li > **1**′@Mg > **1**′@Li (Fig. S22, ESI†).

2.1. Electrical conductivity measurement

To assess their electrical properties, current–voltage (*I–V*) measurements were conducted at room temperature, revealing nonlinear behavior indicative of nonohmic conduction. The measurements were performed using a Keithley 2450 source meter in a two-probe setup with pressed pellets (**1**_P and **1**′_P), which showed significant conductivity variations. Pristine samples, **1**_P and **1**′_P, exhibited conductivities of 3.30×10^{-10} S cm^{-1} and 1.05×10^{-10} S cm^{-1}, respectively (Fig. S23 and S24, ESI†). Doping of metal ions was found to enhance conductivity significantly, reaching up to 10^{-6} S cm^{-1} in pelletized form (Table 1). However, as it is known that the grain boundary issues limit the conductivity in pellet form, the other two approaches were explored: (a) device fabrication on ITO glass and (b) the development of a mixed-matrix membrane (Fig. 4a). These strategies aim to optimize conductivity and functional integration in electronic devices.

Thin films of the compounds were uniformly deposited onto large-area ITO-coated glass substrates, a method commonly employed in industrial device fabrication (Fig. S25, ESI†). The resulting ITO/MOG/Al configurations (Fig. 4g) demonstrate the importance of optimizing film-substrate interactions for enhanced performance in advanced applications. The electrical conductivity of these gel-based materials was analyzed using sandwich–voltage (*I–V*) measurements in a two-probe setup (Fig. 4b). Fabrication and testing were conducted under ambient conditions at room temperature, and the devices were systematically labelled as **1**@Li_T, **1**@Mg_T, **1**′@Li_T, and **1**′@Mg_T. FESEM image, EDAX analysis, and elemental

Table 1 Electrical conductivity values of the pellet, device on ITO glass, and mixed-matrix membrane

Pellet		Device fabrication on ITO glass		Mixed-matrix membrane	
Materials	σ (S cm^{-1})	Materials	σ (S cm^{-1})	Materials	σ (S cm^{-1})
1_P	3.30×10^{-10}	**1**_T	4.40×10^{-10}	**1**_M-60	8.77×10^{-10}
1′_P	1.05×10^{-10}	**1**′_T	1.60×10^{-10}	**1**′_M-60	3.57×10^{-10}
1@Li_P	1.22×10^{-7}	**1**@Li_T	1.70×10^{-6}	**1**@Li_M-60	4.01×10^{-4}
1′@Li_P	5.58×10^{-6}	**1**′@Li_T	1.20×10^{-4}	**1**′@Li_M-60	6.11×10^{-2}
1@Mg_P	3.73×10^{-8}	**1**@Mg_T	1.17×10^{-7}	**1**@Mg_M-60	1.57×10^{-5}
1′@Mg_P	3.38×10^{-7}	**1**′@Mg_T	1.61×10^{-6}	**1**′@Mg_M-60	2.95×10^{-4}

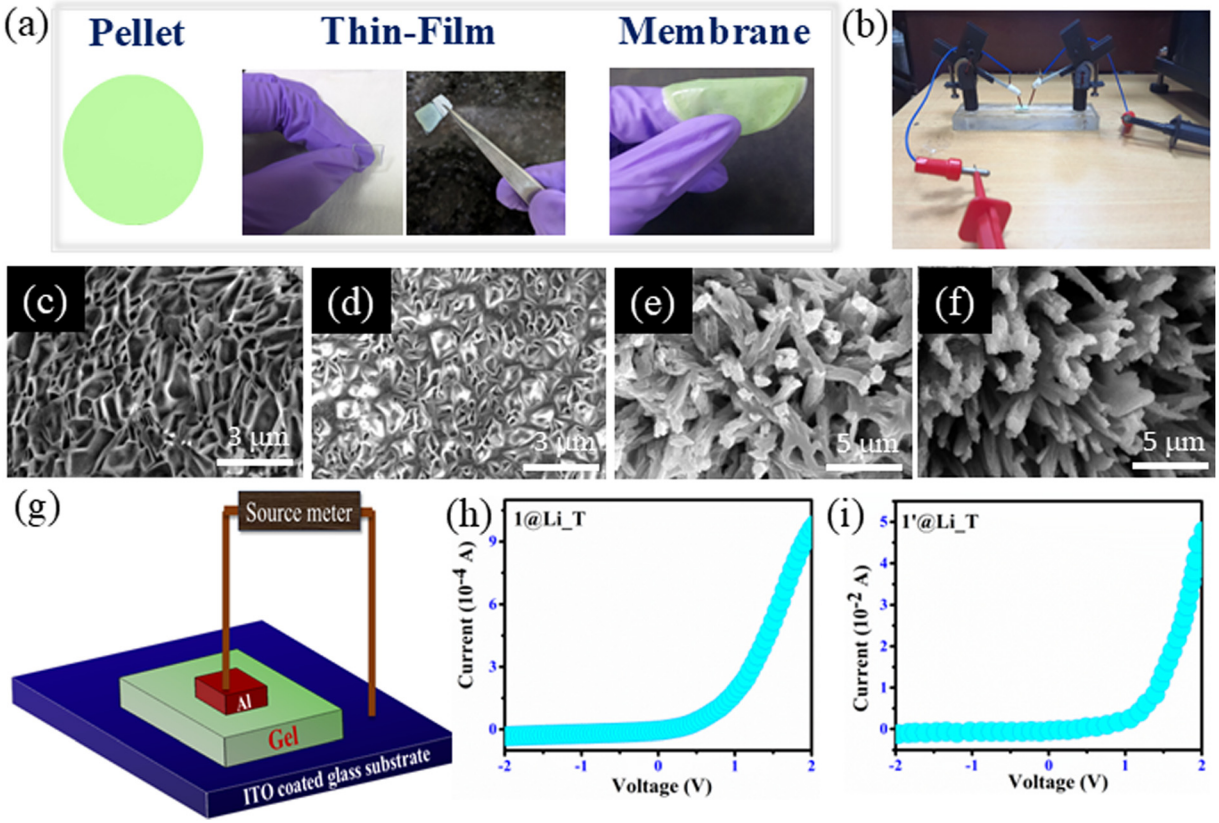

Fig. 4 (a) Three conductivity measurement techniques; (b) conductivity measurement setup; FESEM image on ITO glass (c) **1**@Li, (d) **1**′@Li, (e) **1**@Mg and (f) **1**′@Mg; (g) schematic model of device fabrication on ITO glass; current *vs.* voltage curves for (h) **1**@Li_T and (i) **1**′@Li_T.

mapping confirmed the formation of uniform, homogeneous, and continuous thin films on the ITO substrates, validating the high-quality deposition process (Fig. 4c–f and Fig. S26–S29, ESI†). Notably, the thin-films exhibited significantly improved conductivity properties compared to their pellet form. The measured conductivity values are tabulated in Table 1, they follow the order of **1**′@Li_T > **1**@Li_T > **1**′@Mg_T > **1**@Mg_T > **1**_T > **1**′_T with the conductivity values in the range of 10^{-4} to 10^{-10} S cm^{-1} (Fig. 4h, i and Fig. S30 and S31, ESI†). These findings highlight the substantial conductivity enhancement in the conductivities of Li or Mg-doped MOGs of **1** and **1**′ *via* thin-film fabrication, reinforcing their potential for advanced electronic device applications.

The conductivity of the materials was further evaluated through mixed-matrix membrane (MMM) fabrication using polyvinylidene fluoride (PVDF), and polyvinylpyrrolidone (PVP), chosen for their strong synergy with the gels' organic moieties. MOGs and salt-doped MOGs were well integrated into the PVDF–PVP (1 : 3) matrix at varying loadings. Composite membranes were prepared *via* slurry casting, and membranes containing **1** and **1**′ were labelled as **1**′@X_M-0, **1**′@X_M-20, **1**′@X_M-40, and **1**′@X_M-60 (0, 20, 40, and 60 represent weight percentages of corresponding MOGs, X = Li or Mg and M refers to membrane). Increasing the loading percentage beyond 60% led to the leaching of MOGs and metal salts into the solution. For comparison, a blank PVDF–PVP membrane was also prepared, exhibiting high transparency. However, as the MOG loading increased, the membranes became progressively opaque (Fig. 5a and Fig. S32 and S33, ESI†). Despite this change, the composite membranes remained mechanically robust, crack-free, and flexible—essential properties for semiconductive applications (Fig. 5c, d and Fig. S34–S36, ESI†). The FTIR spectra show the characteristic peaks of materials as well as the polymers PVDF–PVP, representing the perfect blending of the membrane (Fig. S37 and S38, ESI†). Morphological characterization using FESEM and EDAX (Fig. 5b and Fig. S39–S42, ESI†) confirmed a uniform elemental distribution, indicating homogeneous integration of MOG within the membranes. Without doping the metal salt, the electrical conductivities of MMM integrated **1** or **1**′ were found to be about 10^{-10} S cm^{-1}, reflecting their nonconductive nature, similar to the pellets of pure MOGs (Fig. S44a and S45a, ESI†). Furthermore, the MMM with 60% loaded lithium nitrate was found to also be nonconductive (5.98×10^{-12} S cm^{-1}, Fig. S43, ESI†). However, a remarkable enhancement in conductivity was observed for MMMs integrated with metal-doped MOGs (Fig. S44 and S45, ESI†). Systematic experiments with varying loading percentages of metal-doped MOGs reveal that the conductivities increase with the increase in the percentage of metal-doped MOGs (Table S2, ESI†). The conductivities follow the trend of **1**@Mg_M-60 < **1**′@Mg_M-60 < **1**@Li_M-60 < **1**′@Li_M-60 (Table 1). **1**′@Li_M-60 exhibits higher conductivity

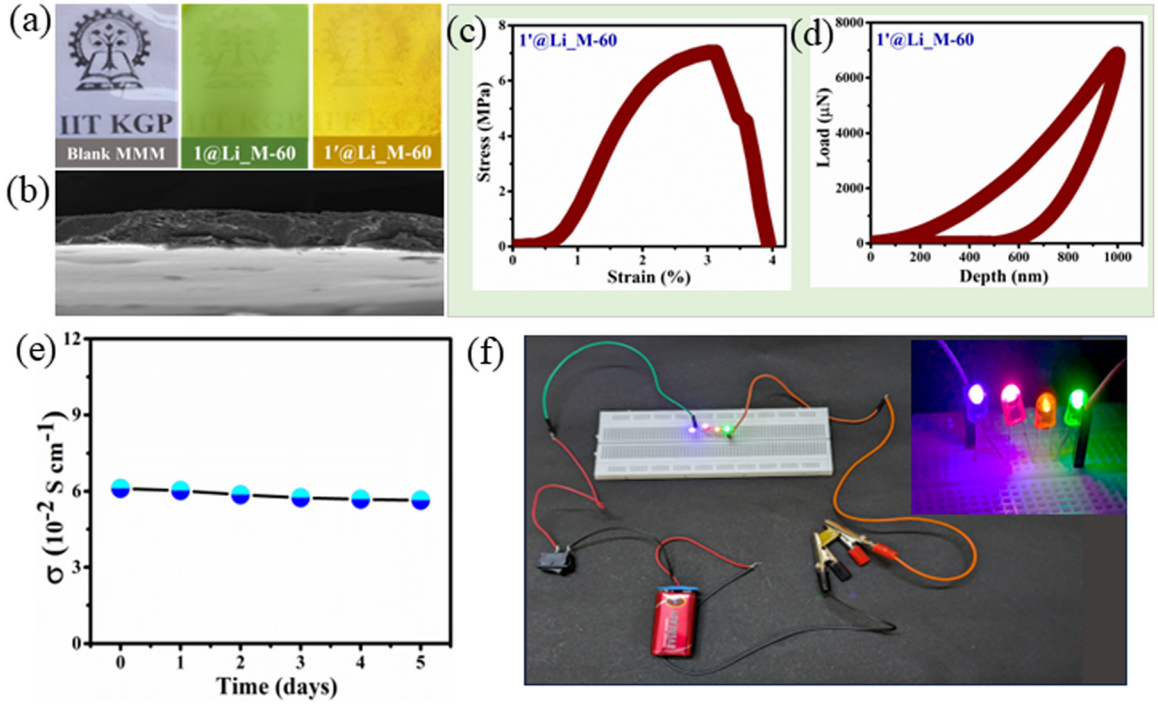

Fig. 5 (a) Optical image of blank MMM, **1**@Li_M-60 and **1**′@Li_M-60; (b) FESEM image of **1**′@Li_M-60; (c) stress–strain curve of **1**′@Li_M-60; (d) load *vs.* depth curve of **1**′@Li_M-60; (e) time-dependent conductivity measurement for **1**′@Li_M-60; (f) illumination of LED light by the fabricated device.

of 6.11×10^{-2} S cm^{-1} at room temperature, which is the highest among all reported MOFs/MOGs based lithium-ion conductivity to date (Table S3, ESI†). It can be noted that the conductivity is enhanced by 10^8-fold by integrating Li doped **1**′ with MMMs when compared with the conductivity of the as-synthesized **1** in pelleted form. The durability test showed that the conductivity of **1**′@Li_M-60 remained stable for 5 days (Fig. 5e). Furthermore, this flexible film was shown to concurrently illuminate LED lights of different colours (Fig. 5f) when inserted within the circuit.

Notably, here an integrated methodology was introduced for conductivity measurement encompassing three distinct techniques: pelletized form, thin-film deposition, and mixed-matrix membrane fabrication. Remarkably, stepwise optimization of these techniques resulted in a dramatic increase in conductivity by one-hundred-million-fold. Grain boundaries act as barriers to charge carrier movement, which can significantly reduce the overall conductivity of a material. In pellets or films, the presence of numerous grain boundaries introduces resistive interfaces, leading to overestimated resistances and underestimated intrinsic conductivity. This issue is particularly severe in pellets, followed by thin films. To address these, the MMM strategy was employed wherein the incorporation of inorganic fillers (MOGs) in combination with a polymer matrix reduces grain boundary density and promotes charge percolation, effectively minimizing intergranular resistance. In addition, membranes offer the best balance between functionality, stability, flexibility, and scalability, making them superior to pellets and thin films for conductivity measurement. This work establishes a new framework for evaluating conductivity in soft materials, offering guidance to minimize grain boundary effects and optimize electrical performance.

We note here that the recent work from our group demonstrated the formation of a one-dimensional double-chain structure by **L** and Cd(II), where carboxylate oxygen atoms bridge two Cd(II) centers while ligand **L** acts as a pendant on both sides of the chain.[32] Based on this structural insight, we propose a

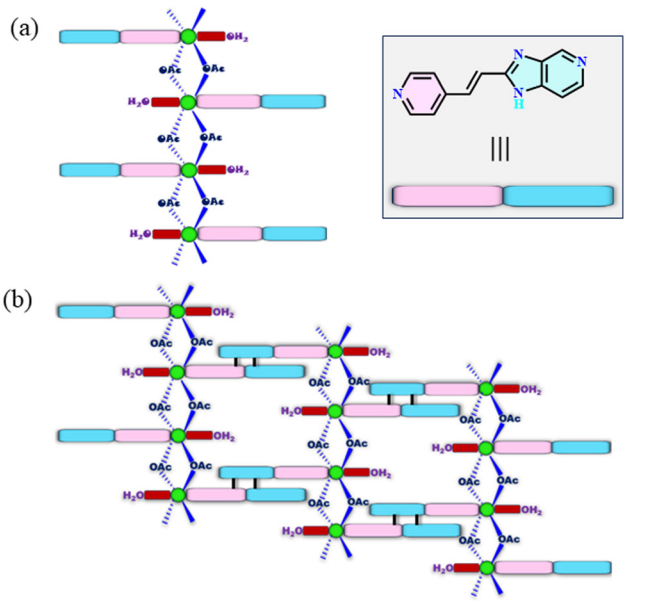

Fig. 6 Schematic representation of the probable structure of the model of MOGs (a) as synthesized and (b) after the photochemical reaction.

probable model for the self-assembly process that leads to gel fiber network formation, both before and after the photochemical [2+2] reaction (Fig. 6). Furthermore, based on this model a favorable pathway for lithium-ion transport, facilitated by synergistic interactions between the gel framework and the polymer matrix was also proposed (Fig. S46, ESI†).

3. Conclusions

In conclusion, this study presents the first-ever example of a Ni(II)-based metal–organic gel exhibiting gel-to-gel transformation *via* photochemical [2+2] cycloaddition and subsequent metal salt doping, leading to significant enhancements in mechanical strength and electrical conductivity. The photochemically transformed MOGs demonstrate remarkable color changes and structural stability, resulting in an unprecedented 51-fold increase in gel rigidity upon Li^+ doping. This exceptional ability to incorporate metal salts and enhance material properties positions these MOGs as highly promising candidates for advanced technological applications. Electrical conductivity measurements reveal that while pristine Ni-MOGs function as insulators, post-irradiation Li^+ doping transforms them into semiconductors. The highest lithium-ion conductivity of 6.11×10^{-2} S cm^{-1} was observed for the **1′**@Li integrated mixed matrix membrane, among all reported MOF/MOG-based materials, underscores the potential for integrating these materials into flexible and scalable electronic devices. The successful fabrication of thin-film and MMM-based devices demonstrates the feasibility of practical applications, overcoming limitations associated with conventional pelleted forms. Furthermore, the ability of these materials to power LEDs highlights their potential for optoelectronic applications, including intuitive signaling in consumer electronics, industrial equipment, and medical devices. The observed tunability of the optical band gaps, influenced by photoreaction and metal ion doping, further supports their versatility in semiconductor technologies. This study establishes a foundation for future exploration of MOG-based semiconductors, emphasizing the transformative impact of structural modifications and dopant incorporation. The insights gained from this work provide new avenues for the development of next-generation flexible and responsive electronic materials, fostering advancements in smart materials, sensors, and energy-efficient optoelectronic devices.

Author contributions

All authors have given approval to the final version of the manuscript.

Conflicts of interest

There are no conflicts to declare.

Data availability

The data supporting this study's findings are included in the article and ESI.†

Acknowledgements

We acknowledge the financial support from DST-SERB (CRG/2022/000606), New Delhi, India. MDD thanks CSIR for the research fellowship.

References

1 A. Mazheika, Y. G. Wang, R. Valero, F. Viñes, F. Illas, L. M. Ghiringhelli, S. V. Levchenko and M. Scheffler, Artificial-intelligence-driven discovery of catalyst genes with application to CO_2 activation on semiconductor oxides, *Nat. Commun.*, 2022, **3**, 419.
2 S. Zhong, B. K. Yap, Z. Zhong and L. Ying, Review on Y6-Based Semiconductor Materials and Their Future Development via Machine Learning, *Crystals*, 2022, **12**, 168.
3 X. Hu, G. Li and J. C. Yu, Design, Fabrication, and Modification of Nanostructured Semiconductor Materials for Environmental and Energy Applications, *Langmuir*, 2010, **26**, 3031–3039.
4 P. Verma and D. G. Truhlar, HLE17: An Improved Local Exchange–Correlation Functional for Computing Semiconductor Band Gaps and Molecular Excitation Energies, *J. Phys. Chem. C*, 2017, **121**, 7144–7154.
5 M. A. Worsley, P. J. Pauzauskie, T. Y. Olson, J. Biener, J. H. Satcher Jr and T. F. Baumann, Synthesis of Graphene Aerogel with High Electrical Conductivity, *J. Am. Chem. Soc.*, 2010, **132**, 14067–14069.
6 G. Skorupskii, K. N. Le, D. L. M. Cordova, L. Yang, T. Chen, C. H. Hendon, M. Q. Arguilla and M. Dincă, Porous lanthanide metal-organic frameworks with metallic conductivity, *Sciences*, 2022, **119**, e2205127119.
7 B. Dhara, S. S. Nagarkar, J. Kumar, V. Kumar, P. K. Jha, S. K. Ghosh, S. Nair and N. Ballav, Increase in Electrical Conductivity of MOF to Billion-Fold upon Filling the Nanochannels with Conducting Polymer, *J. Phys. Chem. Lett.*, 2016, **7**, 2945–2950.
8 N. Behabtu, C. C. Young, D. E. Tsentalovich, O. Kleinerman, X. Wang, A. W. Ma, E. A. Bengio, R. F. ter Waarbeek, J. J. de Jong, R. E. Hoogerwerf, S. B. Fairchild, J. B. Ferguson, B. Maruyama, J. Kono, Y. Talmon, Y. Cohen, J. M. Otto and M. Pasquali, Strong, light, multifunctional fibers of carbon nanotubes with ultrahigh conductivity, *Science*, 2013, **339**, 182–186.
9 A. B. Bogeat, M. A. Franco, C. F. González, A. M. García and V. G. Serrano, Electrical conductivity of activated carbon–metal oxide nanocomposites under compression: a comparison study, *Phys. Chem. Chem. Phys.*, 2014, **16**, 25161–25175.
10 Y. Wang, L. Zhu, G. Niu and J. Mao, Conductive Al Alloys: The Contradiction between Strength and Electrical Conductivity, *Adv. Eng. Mater.*, 2021, **23**, 2001249.

11 S. Roy, S. P. Mondal, S. K. Ray and K. Biradha, A Photoswitchable and Photoluminescent Organic Semiconductor Based On Cation–π and Carboxylate–Pyridinium Interactions: A Supramolecular Approach, *Angew. Chem., Int. Ed.*, 2012, **51**, 12012–12015.
12 F. Al-dolaimy, M. H. Kzar, S. A. Hussein, A. H. Dakheel, M. F. Ramadan, A. S. Abdulwahid, F. A. Rasen, M. L. Shaghnab, A. H. Alawadi, A. Alsalamy and H. Bahir, Advancements in Exploring Metal-Organic Gels: Structure, Synthesis, and Characterization with a Focus on Preparation Conditions, *J. Clust. Sci.*, 2024, **35**, 741–763.
13 P. Sutar and T. K. Maji, Coordination polymer gels: soft metal–organic supramolecular materials and versatile applications, *Chem. Commun.*, 2016, **52**, 8055–8074.
14 S. Samai and K. Biradha, Chemical and Mechano Responsive Metal–Organic Gels of Bis(benzimidazole)-Based Ligands with Cd(II) and Cu(II) Halide Salts: Self Sustainability and Gas and Dye Sorptions, *Chem. Mater.*, 2012, **24**, 1165–1173.
15 S. Ganta and D. K. Chand, Discrete and Polymeric Self-Assembled Palladium(II) Complexes as Supramolecular Gelators, *Chem. – Asian J.*, 2018, **13**, 3777–3789.
16 S. I. Stupp and L. C. Palmer, Supramolecular Chemistry and Self-Assembly in Organic Materials Design, *Chem. Mater.*, 2014, **26**, 507–518.
17 S. Ganta and D. K. Chand, Nanoscale metallogel via self-assembly of self-assembled trinuclear coordination rings: multi-stimuli-responsive soft materials, *Dalton Trans.*, 2015, **44**, 15181–15188.
18 J. Zhang and C.-Y. Su, Metal-organic gels: From discrete metallo gelators to coordination polymers, *Coord. Chem. Rev.*, 2013, **257**, 1373–1408.
19 H. Sun, S. Wang, F. Yang, M. Tan, L. Bai, P. Wang, Y. Feng, W. Liu, R. Wang and X. He, Conductive and antibacterial dual-network hydrogel for soft bioelectronics, *Mater. Horiz.*, 2023, **10**, 5805.
20 D. Liu, C. Huyan, Z. Wang, Z. Guo, X. Zhang, H. Torun, D. Mulvihill, B. B. Xu and F. Chen, Conductive polymer based hydrogels and their application in wearable sensors: a review, *Mater. Horiz.*, 2023, **10**, 2800.
21 S. Panja and D. J. Adams, Stimuli-responsive dynamic transformations in supramolecular gels, *Chem. Soc. Rev.*, 2021, **50**, 5165–5200.
22 S. Liang, M. B. Al-Handawi, T. Chen, P. Naumov and L. Zhang, Hollow Hydrogels for Excellent Aerial Water Collection and Autonomous Release, *Angew. Chem., Int. Ed.*, 2025, **64**, e202415936.
23 R. Contreras-Montoya, L. Á. de Cienfuegos, J. A. Gavira and J. W. Steed, Supramolecular gels: a versatile crystallization toolbox, *Chem. Soc. Rev.*, 2024, **53**, 10604–10619.
24 S. Li, Y. Zeng, W. Hou, W. Wan, J. Zhang, Y. Wang, X. Du and Z. Gu, Photo-responsive photonic hydrogel: in situ manipulation and monitoring of cell scaffold stiffness, *Mater. Horiz.*, 2020, **7**, 2944.
25 S. Amirthalingam, A. K. Rajendran, Y. G. Moon and N. S. Hwang, Stimuli-responsive dynamic hydrogels: design, properties and tissue engineering applications, *Mater. Horiz.*, 2023, **10**, 3325.
26 C. D. Jones and J. W. Steed, Gels with sense: supramolecular materials that respond to heat, light, and sound, *Chem. Soc. Rev.*, 2016, **45**, 6546–6596.
27 M. O. M. Piepenbrock, G. O. Lloyd, N. Clarke and J. W. Steed, Metal- and Anion-Binding Supramolecular Gels, *Chem. Rev.*, 2010, **110**, 1960–2004.
28 G. O. Lloyd and J. W. Steed, Anion-tuning of supramolecular gel properties, *Nat. Chem.*, 2009, **1**, 437–442.
29 X. Yang, G. Zhang and D. Zhang, Stimuli-responsive gels based on low molecular weight gelators, *J. Mater. Chem.*, 2012, **22**, 38–50.
30 A. Das, M. R. Molla, B. Maity, D. Koley and S. Ghosh, Hydrogen-Bonding Induced Alternate Stacking of Donor (D) and Acceptor (A) Chromophores and their Supramolecular Switching to Segregated States, *Chem. – Eur. J.*, 2012, **18**, 9849–9859.
31 A. Garai, A. Goswami and K. Biradha, In situ conversion of a MOG to a crystalline MOF: a case study on solvent-dependent gelation and crystallization, *Chem. Commun.*, 2022, **58**, 11414–11417.
32 M. D. Dawn, S. Roy, A. Garai, S. Banerjee and K. Biradha, Superprotonic Conductivity by Synergistic Blending of Coordination Polymers with Organic Polymers: Fabrication of Durable and Flexible Proton Exchange Membranes, *ChemSusChem*, 2025, **18**, e202401463.
33 D. Ke, C. Zhan, A. D. Li and J. Yao, Morphological Transformation between Nanofibers and Vesicles in a Controllable Bipyridine–Tripeptide Self-Assembly, *Angew. Chem., Int. Ed.*, 2011, **50**, 3715–3719.
34 C. Mahendar, M. K. Dixit, Y. Kumar and M. Dubey, d-(+)-Glucose-triggered metallogel to metallogel transition, *J. Mater. Chem. C*, 2020, **8**, 11008–11012.
35 J. M. Paulusse and R. P. Sijbesma, Molecule-based rheology switching, *Angew. Chem., Int. Ed.*, 2006, **45**, 2334–2337.
36 M. Shirakawa, N. Fujita and S. A. Shinkai, A Stable Single Piece of Unimolecularly π-Stacked Porphyrin Aggregate in a thixotropic Low Molecular Weight Gel: A One-Dimensional Molecular Template for Polydiacetylene Wiring up to Several Tens of micrometers in Length, *J. Am. Chem. Soc.*, 2005, **127**, 4164–4165.
37 P. Xie and R. Zhang, Liquid crystal elastomers, networks and gels: advanced smart materials, *J. Mater. Chem.*, 2005, **15**, 2529–2550.
38 Q. Chen, Y. Feng, D. Zhang, G. Zhang, Q. Fan, S. Sun and D. Zhu, Light-Triggered Self-Assembly of a Spiropyran-Functionalized Dendron into Nano-/Micrometer-Sized Particles and Photoresponsive Organogel with Switchable Fluorescence, *Adv. Funct. Mater.*, 2010, **20**, 36–42.
39 X. Jia, T. Xiao, Z. Hou, L. Xiao, Y. Qi, Z. Hou and J. Zhu, Chemically Responsive Photonic Crystal Hydrogels for Selective and Visual Sensing of Thiol-Containing Biomolecules, *ACS Omega*, 2019, **4**, 12043–12048.
40 B. P. Krishnan and K. M. Sureshan, Topochemical Azide−Alkyne Cycloaddition Reaction in Gels: Size-Tunable Synthesis of Triazole-Linked Polypeptides, *J. Am. Chem. Soc.*, 2017, **139**, 1584–1589.

41 S. Samai, P. Ghosh and K. Biradha, Does crystal or gel matter to stereochemistry of a reaction? Silver complexation-promoted solid-state [2 + 2] reaction of an unsymmetrical olefin, *Chem. Commun.*, 2013, **49**, 4181–4183.

42 S. K. Konavarapu, A. Dey, A. Garai and K. Biradha, Self-Sorting of Metal–Organic Polymeric Assemblies in Gels: Selective Templation and Catalysis of Homodimers, *Chem. – Eur. J.*, 2018, **24**, 5760–5764.

43 X. Wang, P. Duan and M. Liu, Organogelation-Controlled Topochemical [2 + 2] Cycloaddition and Morphological Changes: From Nanofiber to Peculiar Coaxial Hollow Toruloid-Like Nanostructures, *Chem. – Eur. J.*, 2013, **19**, 16072–16079.

44 X. Wang and M. Liu, Vicinal Solvent Effect on Supramolecular Gelation: Alcohol Controlled Topochemical Reaction and the Toruloid Nanostructure, *Chem. – Eur. J.*, 2014, **20**, 10110–10116.

45 S. Kirchhof, F. P. Brandl, N. Hammer and A. M. Goepferich, Investigation of the Diels–Alder reaction as a cross-linking mechanism for degradable poly(ethylene glycol) based hydrogels, *J. Mater. Chem. B*, 2013, **1**, 4855–4864.

46 L. Hsu, G. L. Cvetanovich and S. I. Stupp, Peptide Amphiphile Nanofibers with Conjugated Polydiacetylene Backbones in Their Core, *J. Am. Chem. Soc.*, 2008, **130**, 3892–3899.

47 K. I. Aoki, M. Kudoa and N. Tamaoki, Novel Odd/Even Effect of Alkylene Chain Length on the Photopolymerizability of Organogelators, *Org. Lett.*, 2004, **6**, 4009–4012.

48 M. Masuda, T. Hanada, Y. Okada, K. Yase and T. Shimizu, Polymerization in Nanometer-Sized Fibers: Molecular Packing Order and Polymerizability, *Macromolecules*, 2000, **33**, 9233–9238.

49 O. J. Dautel, M. Robitzer, J. P. Lère-Porte, F. Serein-Spirau and J. J. Moreau, Self-Organized Ureido Substituted Diacetylenic Organogel. Photopolymerization of One-Dimensional Supramolecular Assemblies to Give Conjugated Nanofibers, *J. Am. Chem. Soc.*, 2006, **128**, 16213–16223.

50 R. Mandal, A. Garai and K. Biradha, Solid or gel? Which one works better for [2 + 2] photochemical polymerization in pyridine appended flexible phenylene 1, 4-bis-olefins by Ag(i) templation?, *Dalton Trans.*, 2019, **48**, 17456–17460.

51 R. Mandal and K. Biradha, Photochemical [2 + 2] polymerization of metal-organic gels of a rigid and angular diene with silver-salts of diverse anions: selective dye-sorption and luminescence by xerogels, *Dalton Trans.*, 2020, **49**, 13744–13752.

52 S. Sultana, R. Mandal and K. Biradha, Photo-responsive metal–organic gels of rigid phenylene-1, 3-di-substituted angular dienes with metal halides: gel-to-gel transformations triggered by [2+ 2] polymerization, *Dalton Trans.*, 2024, **53**, 4797–4804.

53 S. Roy, S. P. Mondal and K. Biradha, Multifunctional white-light-emitting metal–organic gels with a sensing ability of nitrobenzene, *ACS Appl. Mater. Interfaces*, 2014, **6**, 11493–11501.

54 R. Moi, K. Nath, D. Ghosh and K. Biradha, Metal-Organic Gels of Tris-tetrazole-tri-amido Molecule with Co(II) and Ni(II) as Effective Electrocatalysts for Oxygen Evolution Reaction: Effect of Metal Ion, Porosity and Morphology on the Catalytic Activity of MOGs, *ChemCatChem*, 2023, **15**, e202300694.

55 P. Verma, F. A. Rahimi, D. Samanta, A. Kundu, J. Dasgupta and T. K. Maji, Visible-Light-Driven Photocatalytic CO_2 Reduction to CO/CH_4 Using a Metal–Organic "Soft" Coordination Polymer Gel, *Angew. Chem., Int. Ed.*, 2022, **61**, e202116094.

56 W. Wu, A. M. Kirillov, X. Yan, P. Zhou, W. Liu and Y. Tang, Enhanced Separation of Potassium Ions by Spontaneous K + -Induced Self-Assembly of a Novel Metal–Organic Framework and Excess Specific Cation–π Interactions, *Angew. Chem.*, 2014, **126**, 10825–10829.

57 B. Dhara and N. Ballav, In situ generation of conducting polymer in a redox active metal–organic gel, *RSC Adv.*, 2013, **3**, 4909–4913.

58 J. Puigmartí-Luis, V. Laukhin, A. Perez del Pino, J. Vidal-Gancedo, C. Rovira, E. Laukhina and D. B. Amabilino, Supramolecular Conducting Nanowires from Organogels, *Angew. Chem., Int. Ed.*, 2007, **46**, 238–241.

59 D. Vallejo-Sánchez, P. Amo-Ochoa, G. Beobide, O. Castillo, M. Froeba, F. Hoffmann, A. Luque, P. Ocon and S. Pérez-Yáñez, Chemically Resistant, Shapeable, and Conducting Metal-Organic Gels and Aerogels Built from Dithiooxamidato Ligand, *Adv. Funct. Mater.*, 2017, **27**, 1605448.

60 A. Goswami, D. Ghosh, A. Garai, D. Pradhan and K. Biradha, Bimetallic Organic Frameworks via In Situ Solvothermal Sol–Gel–Crystal and Sol–Crystal Transformation as Durable Electrocatalysts for Oxygen Reduction Reaction, *Inorg. Chem.*, 2024, **63**, 7303–7313.

61 M. D. Dawn, K. Nath, S. Saha, P. K. Roy, M. Mandal and K. Biradha, Enhancing the Sensitivity of a Water Stable MOF as a H_2S Gas Sensor by the Fabrication of Mixed-Matrix Membrane, *Mater. Adv.*, 2023, **4**, 5730–5739.

62 J. An, J. Oh, U. Kurakula, D. H. Lee, A. Choudhury, E. Lee, R. Medishetty and I.-H. Park, Solid-State Structural Transformation in Zn(II) Metal–Organic Frameworks in a Single-Crystal-to-Single-Crystal Fashion, *Nanomaterials*, 2023, **13**, 2319.

63 S. Bedi, K. Bharti, D. Banerjee and K. Biradha, Ten-Million-Fold Increase in the Electrical Conductivity of a MOF by Doping of Iodine Into MOF Integrated Mixed Matrix Membrane, *Small*, 2024, **20**, 2406701.

64 B. M. Wiers, M. L. Foo, N. P. Balsara and J. R. Long, A Solid Lithium Electrolyte via Addition of Lithium Isopropoxide to a Metal–Organic Framework with Open Metal Site, *J. Am. Chem. Soc.*, 2011, **133**, 14522–14525.

65 S. S. Park, Y. Tulchinsky and M. Dincă, Single-Ion Li^+, Na^+, and Mg^{2+} Solid Electrolytes Supported by a Mesoporous Anionic Cu-Azolate Metal-Organic Framework, *J. Am. Chem. Soc.*, 2017, **139**, 13260–13263.

66 K. Nath, A. B. Rahaman, R. Moi, K. Maity and K. Biradha, Porous Li-MOF as a solid-state electrolyte: exploration of lithium ion conductivity through bio-inspired ionic channels, *Chem. Commun.*, 2020, **56**, 14873–14876.

67 Z. Liu, P. Liu, L. Tian, J. Xiao, R. Cui and Z. Liu, Significantly enhancing the lithium-ion conductivity of solid-state electrolytes via a strategy for fabricating hollow metal–organic frameworks, *Chem. Commun.*, 2020, **56**, 14629–14632.

68 L. Shen, H. B. Wu, F. Liu, J. L. Brosmer, G. Shen, X. Wang, J. I. Zink, Q. Xiao, M. Cai, G. Wang and Y. Lu, Creating Lithium-Ion Electrolytes with Biomimetic Ionic Channels in Metal–Organic Frameworks, *Adv. Mater.*, 2018, **30**, 1707476.
69 I. Virt, Recent Advances in Semiconducting Thin Films, *Coatings*, 2023, **13**, 79.
70 S. Samai and K. Biradha, Coordination Polymers of Flexible Bis(benzimidazole) Ligand: Halogen Bridging and Metal Arene Interactions, *Cryst. Growth Des.*, 2011, **11**, 5723–5732.
71 H. Liu, Y. Wu, Y. Li, X. Xie, P. Li, B. Du and L. Li, Effect of different valence metal cations on the gel characteristics and microstructure of Inca peanut albumin gels, *Food Hydrocolloids*, 2024, **151**, 109783.
72 X. Lu, Z. Lu, L. Yin, Y. Cheng and L. Li, Effect of preheating temperature and calcium ions on the properties of cold-set soybean protein gel, *Food Res. Int.*, 2010, **43**, 1673–1683.
73 H. Zhou, X. Hu, X. Xiang and D. J. McClements, Modification of textural attributes of potato protein gels using salts, polysaccharides, and transglutaminase: Development of plant-based foods, *Food Hydrocolloids*, 2023, **144** 108909.